Journal of Crystal Growth 555 (2021) 125958

Contents lists available at ScienceDirect

Journal of Crystal Growth

journal homepage: www.elsevier.com/locate/jcrysgro

Analysis of faceted solidification in the horizontal ribbon growth crystallization process

Alireza Pirnia, Brian T. Helenbrook *

Department of Mechanical and Aeronautical Engineering, Clarkson University, 8 Clarkson Ave., Box 5725, Potsdam, NY 13699, USA

ARTICLE INFO

Communicated by Chung wen Lan

Keywords:
A1. Growth model
A1. Heat transfer
A1. Interfaces
A1. Solidification kinetics
A2. Horizontal ribbon growth
B3. Solar cells

ABSTRACT

Horizontal ribbon growth (HRG), in which a thin sheet of solidified material is pulled horizontally from the surface of a molten pool, is proposed as an efficient technique for growth of single-crystal silicon sheets. Despite recent results, some details of the process are still not understood, in particular the solidification mechanism at the triple junction point (TJP) where the solid, the liquid, and the surrounding gas meet. The solidification mechanism in the HRG process is investigated in this paper both analytically and numerically, incorporating the solidification kinetics that lead to faceted growth. The conventional solid–liquid problem in the HRG process is formulated analytically in the vicinity of the triple junction point (TJP). The temperature distribution is obtained for the liquid and solid regions as a function of the underlying parameters of the HRG process, such as the material properties, the ribbon pull speed, and the cooling heat fluxes. Using the analytical results, the TJP temperature, the facet length, interfacial temperature gradients, and liquid supercooling can be predicted. The analytical formulation is validated against accurate numerical simulations of the same problem, showing a good agreement in predicting the temperature gradients and the facet growth. The findings of this study suggest that using the analytical model, the behavior of the solid ribbon and the existence of a supercooled region in the liquid in the HRG process can be predicted without the need for numerical simulations. The model also gives criteria for optimal performance of the HRG process.

1. Introduction

Crystal growth techniques are used for the production of silicon wafers for application in photovoltaic devices such as solar cells [1,2]. There are various techniques for growing crystals such as Czochralski [3,4], edge-defined film-fed (EFG) [5,6], and horizontal ribbon growth (HRG) [7–9]. The Czochralski process, in which large diameter ingots are made by vertical crystal growth, is the most commercially used. However, relatively slow growth speeds and large kerf losses during wafer cutting reduce the efficiency of this process [10]. In contrast, HRG methods, in which wide thin sheets of materials are pulled horizontally from the cooled and solidified surface of a molten pool, are reported to achieve much larger growth speeds and do not suffer from cutting losses [11,12]. However, the gaps of knowledge of the physics involved in the HRG process have resulted in a considerable difference between theoretical expectations and experimental observations, hindering attempts at commercializing this technique [13].

The solidification front in any solidification process terminates at a point (or line) in contact with a solid wall [14–17], or a gas domain [18–20]. The termination point (line) is usually called a triple junction [21]. In HRG processes, in particular, the shape and temperature distribution of the solidification front at the triple junction can have a significant influence on the stability and maximum performance of the process [22,23].

Despite several attempts at theoretical analysis of the HRG process and its stability in various configurations [8,11,23–26], very few studies have analyzed the physics of the triple junction in detail. Anderson and Davis [27] solved the Stefan problem and obtained the flow and temperature fields in the vicinity of the triple junction. They concluded that the solidification front is perpendicular to the free surface at the junction when the free surface is adiabatic. The same conclusion can be made for droplet solidification problems where the heat transfer is mainly through the solid–liquid interface [14]. Helenbrook [22] included the heat transfer through the gas domain in the Stefan problem. He found that a non-zero wedge angle, *i.e.*, the angle between the solidification front and the free surface, is only possible if there is a jump in heat transfer at the triple junction or when there is a non-zero growth angle (*i.e.*, the angle between the growth direction of the triple junction point

* Corresponding author.
E-mail address: bhelenbr@clarkson.edu (B.T. Helenbrook).

https://doi.org/10.1016/j.jcrysgro.2020.125958
Received 20 August 2020; Received in revised form 9 November 2020; Accepted 13 November 2020
Available online 22 November 2020

and the incoming free surface tangent). A jump in heat transfer is highly probable due to different radiative emissivity between the liquid and the solid phases of materials such as silicon. The formed wedge angle at the triple junction was found to be a function of the ribbon pull speed, the latent heat release rate, the heat removal jump, and the growth angle [22].

In contrast to the theoretical predictions, experimental observations of the HRG process have shown that the solidification front close to the triple junction is more like a facet that is usually aligned with {1 1 1} planes, and not a wedge [28,29]. For example, Helenbrook et al. [28] took a side-view picture of a sample ribbon after shutting off the cooling jet and showed that the ribbon leading edge is planar, making a 55° angle with the ribbon top surface (refer to Fig. 3 of the reference). Moreover, the experiments have all shown a finite limit for the pull speed [11,12], unlike predictions from wedge-based theories. One important distinction between the aforementioned analytical studies and the experiments is that the temperature at the solidification front is assumed to be constant and equal to the equilibrium melting temperature in the analyses. However, this assumption is only valid if the solidification kinetics are fast [28].

Solidification kinetics play an important role in the formation of the solidification front in the HRG processes. Kinetic undercooling models have been used in different numerical simulations for the evaluation of interfacial temperatures and supercooled regions [30,31]. For example, Helenbrook et al. [28] showed that there is a supercooled region right in front of the facet formed in the vicinity of the triple junction where 2D nucleation and step propagation mechanisms are dominant. They also showed that increasing the pull speed retracts the triple junction (the leading edge of the ribbon) away from the cooling region. This trend continues until a turning point is reached in the variation of the converged triple juction position versus the pull speed, after which dendritic growth occurs and there is no stable steady solution. As such, any theoretical modeling of the HRG process requires the inclusion of solidification kinetics.

In this study, the HRG process is investigated analytically and numerically. A model is formulated that incorporates the solidification kinetics and focuses on the vicinity of the triple junction, where the solidification process and the formation of the solid ribbon are initiated. The findings of this work can be extended to other similar solidification processes as long as a triple junction exists in the domain. The manuscript is organized as follows: The HRG configuration is described in Section 2. An analytical formulation for the solid–liquid temperature field in the vicinity of the triple junction is obtained in Section 3 by inclusion of the solidification kinetics, which is explained in Section 4. A procedure for numerical simulation of the same problem is discussed in Section 5. The results of the analytical model are compared and validated against the numerical solutions in Section 6 and a discussion of the model and the criteria for liquid supercooling is provided.

2. Problem description

In the HRG configuration, all the interfaces (solid–liquid, solid–gas, and liquid–gas) are joined at the triple junction located at the solid leading edge. Fig. 1(a) shows a schematic of the liquid domain, Ω_l, and the floating solid sheet, Ω_s. It is assumed in this configuration that the width of the sheet, W, is much larger than the crucible depth, d, such that the problem can be considered as two-dimensional and the triple junction can be assumed to be a point (TJP). A closeup view of the solidification front in the vicinity of the TJP is shown in Fig. 1(b), where three coordinate systems are defined with their origin positioned at the TJP. Coordinate x is aligned with the solid–gas interface. The x^*-y^* and the polar r-θ coordinates are aligned with the solid–liquid interface (the solidification front), such that y^* is normal to the interface and facing the solid domain, r is the distance from the TJP, and θ is the angle relative to the interface with a counter-clockwise (CCW) positive sign.

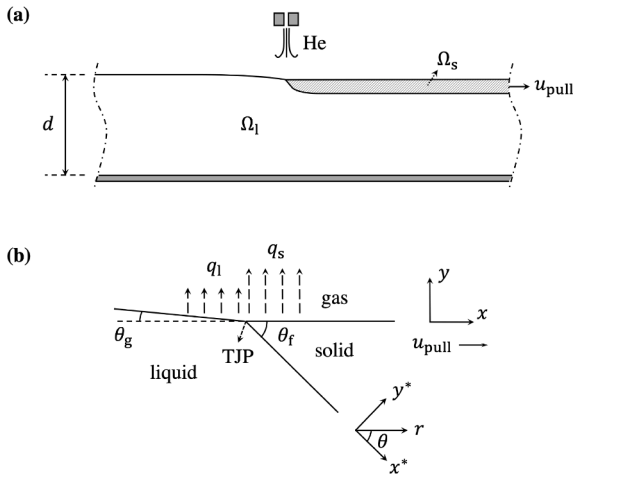

Fig. 1. Schematic of the HRG crystallization with a) configuration of the domains, b) close view of the solidification front in the vicinity of TJP and the prescribed coordinate systems.

The solid ribbon is pulled in the x-direction in Fig. 1, which is aligned with a [1 0 0] crystal direction, with a pulling speed of u_{pull}. In the steady-state condition, the liquid solidification balances the pulled solid mass, such that the TJP is stationary. The problem is analyzed in the limit of $r < \epsilon$, where $\epsilon \ll d$, and therefore, all interfaces can be approximated as straight lines. In the $r < \epsilon$ limit, the solidification front forms a facet with a constant facet angle of θ_f. In all of the studied cases in this work, it is assumed that the crystal is seeding with the [1 0 0] direction oriented in the ribbon pulling direction and a (1 1 1) facet plane 55deg from the x-direction. The liquid surface also forms a growth angle of θ_g with the $-x$ direction. In the polar coordinates, the solid–gas interface is positioned at $\theta = \theta_f$ and the liquid–gas interface (the free surface) is positioned at $\theta = \theta_f + \pi - \theta_g$.

Heat is removed through the gas domain by convection and radiation from the solid and the liquid top surfaces. A cold helium jet provides the convection heat removal, which is assumed continuous across the TJP. Heat is also radiated to an assumed cold far-field. Because the emissivities of liquid and solid materials are usually different (*e.g.*, emissivity of solid silicon is larger than its liquid), there is a jump in the radiated heat at the TJP location, as shown in Fig. 1(b). Since the problem is investigated in the $r < \epsilon$ limit, the heat flux from the liquid surface is assumed constant and equal to q_l, and equivalently, constant and equal to q_s from the solid surface. Due to the jump in radiation, q_l and q_s are not equal.

3. Analytical formulations

3.1. Governing equations

The governing equation for heat balance in this problem in both the liquid (Ω_l) and solid (Ω_s) domains can be stated as

$$\frac{\partial(\rho_i c_i T_i)}{\partial t} + \nabla\cdot(\rho_i \boldsymbol{u}_i c_i T_i) + \nabla\cdot(-k_i \nabla T_i) = 0, \tag{1}$$

where subscript $i = l, s$ refers to either of the domains, T and $\boldsymbol{u}$ are the temperature field and the velocity vector, respectively, and ρ,c, and k are the density, specific heat, and thermal conductivity of each domain, respectively.

In order to simplify Eq. (1), a few assumptions are made. The problem is assumed to reach a steady-state condition, and therefore, the first term from the left vanishes. The material density is assumed constant and equal for both the liquid and the solid close to the TJP in the $r < \epsilon$ limit. This means the velocity field is continuous across the solidification interface according to the continuity equation. As such, the liquid velocity close to the TJP is equal to the solid velocity, which is equal to

$u_{\text{pull}}\hat{i}$, where $\hat{i}$ is the unit vector in the x-direction (see Fig. 1).

After simplifying and substituting the non-dimensional variables of $x' = x/\epsilon, y' = y/\epsilon$, and $T' = (T - T_m)/T_m$, where ϵ is the radius of the small region of interest near the TJP and T_m is the equilibrium melting temperature, Eq. (1) can be re-written as

$$\text{Pe}_i \frac{dT_i'}{dx'} - \nabla^2 T_i' = 0, \tag{2}$$

where $\text{Pe}_i = \rho c_i u_{\text{pull}} \epsilon / k_i$ is the Peclet number, which is negligible in the $\epsilon \to 0$ limit. As such, the convective term can be ignored for the solution of the temperature distribution in the vicinity of the TJP and the governing equation is reduced to $\nabla^2 T_i = 0$.

In order to solve the Laplacian equation for temperature, the boundary conditions must be specified. At the liquid–gas and solid–gas interfaces, the boundary conditions are $-k_i \nabla T_i \cdot \hat{n}_i = q_i$, where q_i is the heat flux through the solid or the liquid surfaces and $\hat{n}_i$ in the unit vector of the outward normal to these boundaries. At the solidification interface, the net heat flux normal to the boundary must balance the rate of heat release due to the solidification process, such that

$$[[-k_i \nabla T_i \cdot \hat{n}_i]] = \dot{m} L_f, \tag{3}$$

where the double-brackets indicate the jump in heat flux at the interface, L_f is the latent heat of fusion, and $\dot{m} = \rho(\boldsymbol{u}_s - \boldsymbol{u}_I)\cdot\hat{n}_s$ is the rate of mass added to the solid normal to the liquid–solid interface, where $\boldsymbol{u}_s$ and $\boldsymbol{u}_I$ are the solid and interface velocity vectors, respectively, and $\hat{n}_s$ is the outward unit normal to the solid at the interface. In the steady-state condition in the configuration of interest, $\boldsymbol{u}_I = 0$ and $\boldsymbol{u}_s = u_{\text{pull}}\hat{i}$.

3.2. Linear approximation

At leading order, it is assumed that the temperature very close to the TJP ($r < \epsilon$) is a linear function of the x^* and y^* coordinates. Defining a new variable of $\Theta = T - T_{\text{TJP}}$, where T_{TJP} is the temperature at the TJP, the distribution of temperature difference from the TJP in both domains can be expressed as

$$\Theta_i = a_i^* x^* + b_i^* y^*, \tag{4}$$

where a_i^* and b_i^* are constants for each domain. For the temperature distribution to be continuous across the solidification front, where $y^* = 0$, we should have $a_s^* = a_l^* = a^*$.

For simplicity, the liquid–gas interface is assumed horizontal, which means that the growth angle (θ_g) is equal to zero. Consequently, the boundary conditions at the solid–gas and liquid–gas interfaces with $\hat{n}_s = \hat{n}_l = -\sin(\theta_f)\hat{i}^* + \cos(\theta_f)\hat{j}^*$ can be written as

$$\begin{aligned} k_s\left[a^* \sin(\theta_f) - b_s^* \cos(\theta_f)\right] &= q_s, \\ k_l\left[a^* \sin(\theta_f) - b_l^* \cos(\theta_f)\right] &= q_l. \end{aligned} \tag{5}$$

Similarly, the boundary condition at the solidification front (Eq. (3)) with $\hat{n}_s = -1\hat{j}^*$, $\hat{n}_l = 1\hat{j}^*$, and $\hat{i} = \cos(\theta_f)\hat{i}^* + \sin(\theta_f)\hat{j}^*$ states that

$$b_s^* k_s - b_l^* k_l = -\rho L_f u_{\text{pull}} \sin(\theta_f). \tag{6}$$

3.3. Analytical model of the solid–liquid problem

As shown in Fig. 1, the heat removal rate through the gas domain is uniform on either side of the TJP but is discontinuous at the TJP, usually due to different liquid and solid emissivities. By subtracting the two parts of Eq. (5) and combining with Eq. (6), an expression for a^* can be obtained as

$$a^* = \frac{\rho L_f u_{\text{pull}} \cos(\theta_f)}{k_l - k_s} - \frac{q_s - q_l}{(k_l - k_s)\sin(\theta_f)}. \tag{7}$$

This is the linear temperature gradient along the interface (x^*-direction) required to maintain growth at a constant facet angle. It can be seen that the tangential temperature gradient is a function of the pull speed, the jump in heat flux (not the heat flux magnitudes), the difference in solid and liquid thermal conductivities, and the latent heat.

After substituting the obtained expression for a^* into Eq. (5), the temperature gradient normal to the interface (y^*-direction) in both domains is given by

$$b_i^* = \frac{\rho L_f u_{\text{pull}} \sin(\theta_f)}{k_l - k_s} - \frac{q_s - q_l}{(k_l - k_s)\cos(\theta_f)} - \frac{q_i}{k_i \cos(\theta_f)}. \tag{8}$$

Ultimately, the temperature field close to the TJP can be obtained in the original x-y coordinate system using a coordinate transformation, such that

$$\begin{aligned} T_i = T_{\text{TJP}} &- \frac{q_i}{k_i} y + \\ &\left(\frac{\rho L_f u_{\text{pull}}}{k_l - k_s} - \frac{q_s - q_l}{k_l - k_s}\left[\cot(\theta_f) + \tan(\theta_f)\right] - \frac{q_i}{k_i}\tan(\theta_f)\right) x. \end{aligned} \tag{9}$$

Note that this simplified temperature solution is derived by assuming negligible liquid flow, constant heat fluxes, equal solid and liquid densities, and zero liquid growth angle in the vicinity of the TJP. However, it was observed during additional numerical simulations (not shown here for brevity) that relaxing these assumptions has negligible effects on the solution in the small radius of interest. This is mainly because the convective terms in Eq. (2) can be ignored because of the small Pe in the close proximity of the TJP.

When the temperature gradient in the x direction in Eq. (9) is positive in the liquid domain at the TJP ($dT/dx > 0$), it means a supercooled region exists with the minimum temperature located in the liquid domain. The criteria for liquid supercooling is discussed in detail in Section 6.4. In Eq. (9), the TJP temperature is still unknown, which is obtained by incorporating the solidification kinetics, as explained in the following section.

4. Solidification kinetics

4.1. Solidification mechanisms

It was previously mentioned that the temperature at the solid–liquid interface is not usually equal to the equilibrium melting temperature and depends on the solidification mechanism. There are three solidification mechanisms that can occur at the solid–liquid interface: the two-dimensional (2D) nucleation of crystals on a facet, propagation of steps down the facet face, and roughened growth without any identifiable facet [28].

In this work, a slightly modified version of the kinetics model proposed by Weinstein and Brandon [30] is used for quantifying the three mechanisms. The specific model and its constants are identical to that used by Helenbrook et al. [28]. This model states that the deviation of interface temperature, T_I, from the melting temperature, T_m, is obtained by

$$\Delta T_I = T_I - T_m = K(\theta_{ma}, \Delta T_I)(\boldsymbol{u}_s - \boldsymbol{u}_I)\cdot\hat{n}_s, \tag{10}$$

where K is a solidification kinetic coefficient and θ_{ma}, referred to as the misalignment angle, is the CCW angular deviation of the actual interface from the $\theta = 0$ line. As stated before, $\boldsymbol{u}_I = 0$ in the steady-state condition and $\boldsymbol{u}_s \cdot \hat{n}_s$ is less than or equal to zero in the current configuration.

The kinetic coefficient is composed of the three solidification mechanisms and its value is a function of the local interface condition. Roughened growth occurs in directions away from the facet direction and has a constant kinetic coefficient of $K_{\text{rough}} = 1/0.0126$ [K/(m/s)]. Step propagation occurs along the facet and models the growth of a molecular layer on the facet with a kinetic coefficient that is a function

of θ_{ma} and is given by $K_{step} = K_{sn}/|\sin\theta_{ma}|$, where $K_{sn} = 1/0.63$ [K/(m/s)] is a constant. Lastly, 2D nucleation describes when a new facet layer is initiated. The kinetic coefficient for 2D nucleation is a function of the temperature deviation and is given by $K_{2D} = K_{2Dn}\exp(A_{2Dn}/|\Delta T_I|)$, where $K_{2Dn} = 1/1.5e10$ [K/(m/s)] and $A_{2Dn} = 140$ [K] are constants. The 2D nucleation typically occurs at the coldest location in the liquid, where liquid supercooling is appreciable, and can be as fast as the roughened growth when $|\Delta T_I| > 5$ [K] [29].

Close to the TJP and along the facet, the solidification mechanism with the least kinetic coefficient (K_{2D} or K_{step}) will occur, as a smaller K is more physically probable [30]. Far from the facet at large misalignment angles, the K_{step} expression is no longer valid and roughened growth will occur. As such, the kinetic coefficient should not be less than K_{rough} along the interface. In the analytical and numerical models in this study, it is assumed that the coldest temperature, and consequently 2D nucleation, only occurs at the TJP and therefore $K_{TJP} = K_{2D}$. To effectively model the solidification mechanism along the rest of the solidification front, the following expression is used in this study.

$$K(\theta_{ma}, \Delta T_I) = \max\left(K_{step}, K_{rough}\right). \tag{11}$$

4.2. Faceted solidification

The region of interest in this study is close to the TJP and along the facet, as discussed in Section 3. In this region, the misalignment angle is small ($\theta_{ma} \ll 1$) and $K_{step} \gg K_{rough}$, and therefore, roughened growth does not occur and can be ignored. The solidification is nucleated at the TJP, as it is the only feasible location in this configuration. Therefore, the temperature at the TJP can be obtained from Eq. (10) using the kinetic coefficient for 2D nucleation, such that

$$\Delta T_{TJP} = -K_{2Dn}\exp(-A_{2Dn}/\Delta T_{TJP})u_{pull}\sin(\theta_f). \tag{12}$$

Note that if the actual solidification front deviates from a line with the constant facet angle by θ_{ma} degrees, then the component of pull speed normal to the solidification front is equal to $(\boldsymbol{u}_s - \boldsymbol{u}_I)\cdot\hat{\boldsymbol{n}}_s = -u_{pull}\sin(\theta_f - \theta_{ma})$. However since θ_{ma} is small, it can be ignored in the equation. It can be seen from Eq. (12) that the temperature at the TJP is then only a function of the pull speed.

The nucleated step at the TJP is propagated along the facet by the step propagation mechanism. Combining Eq. (4) with Eq. (10) using the kinetic coefficient for step propagation, the temperature distribution along the facet in the $r \to \epsilon$ limit is governed by

$$T_I(x^*) = T_m - \frac{K_{sn}}{|\sin\theta_{ma}|}u_{pull}\sin(\theta_f - \theta_{ma}) = T_{TJP} + a^* x^*. \tag{13}$$

considering that $\theta_{ma} \ll \theta_f$, the misalignment angle in the vicinity of the TJP can be estimated as

$$\theta_{ma}(x^*) \simeq \frac{K_{sn}u_{pull}\sin(\theta_f)}{T_m - T_{TJP} - a^* x^*}. \tag{14}$$

It can be concluded from Eq. (14) that the misalignment angle becomes large as the interface temperature approaches the equilibrium melting temperature. When θ_{ma} becomes sufficiently large, roughened solidification starts to develop. The misalignment angle at which this transitions occurs can be found by equating K_{rough} and K_{step}, such that $\sin(\theta_{trans}) = K_{sn}/K_{rough}$. Plugging this value into Eq. (14), the location of transition on the solidification front (x^*_{trans}) can be obtained. In this study, x^*_{trans} is defined as the facet length.

5. Numerical procedure

The analytical formulations described in Section 3.3 and Section 4.2 provide an estimation for the temperature distribution and the shape of the solid–liquid interface in the vicinity of the TJP in the HRG configuration. To validate these estimates, a high-order accurate numerical procedure is used that solves the temperature and flow fields in both the liquid and solid domains and determines the interface position while accounting for the solidification kinetics [32].

The employed method is a *hp*-finite element formulation with 4th order approximation polynomials and a triangular arbitrary Lagrangian–Eulerian (ALE) moving mesh. The interface is tracked by the moving mesh and sharp gradients in the domains are resolved using a mesh adaptation algorithm. For the solution of the numerical formulations, an A-stable diagonally implicit Runge–Kutta temporal scheme is used. The temporal and spatial orders of accuracy for this method are reported to be 3 and 5, respectively [32]. For a more detailed description of the numerical procedure refer to references [28,32].

A sample of the initial mesh used in the numerical method for the configuration shown in Fig. 1(a) is displayed in Fig. 2. It can be seen that the solid (Ω_s) and the liquid (Ω_l) domains are non-dimensionalized by the crucible depth, d. The domains are extended by $4d$ from the TJP in both directions to ensure uniform inlet conditions and a stabilized maximum thickness of the ribbon resulting from the fact that the top heat removal and bottom heat addition fluxes balance at either end of the domain. In order to simplify the flow solution, the liquid surface tension is assumed constant, and therefore, the Marangoni effects are ignored. The top boundary of the liquid (the free surface) is set as a slip boundary. The left boundary is set as an inflow and the bottom boundary is set as a moving wall, both with a uniform velocity of u_{pull}. The right boundary of the liquid is defined as an outflow with zero stress condition. With these specified boundary conditions, the entire flow field is uniform and equal to u_{pull}, which is also the specified convective rate for the solid domain.

For the solution of the energy equation, the inflow boundary of the liquid has a Dirichlet thermal boundary condition, which varies linearly from a top point temperature, T_t, to a bottom point temperature, T_b. Both specified temperatures are greater than the melting temperature, T_m. The bottom boundary also has a specified Dirichlet temperature of T_b. The right boundaries of both the liquid and solid domains have Neumann boundary conditions with zero conductive heat flux. The top boundaries have Neumann boundary conditions with a heat removal rate of $q_c(x) + q_r(x)$. In this model, q_c is a continuous distribution for modeling the convective heat transfer by the cooling helium jet located above the solid ribbon (see Fig. 1), and q_r is the radiative heat transfer that is discontinuous at x_{TJP} due to different liquid and solid emissivities. It should be noted that although the TJP is positioned at $x = 0$ in the initial mesh, its location changes during the solution procedure, and therefore, the Neumann boundary condition at the top surfaces is updated in each iteration.

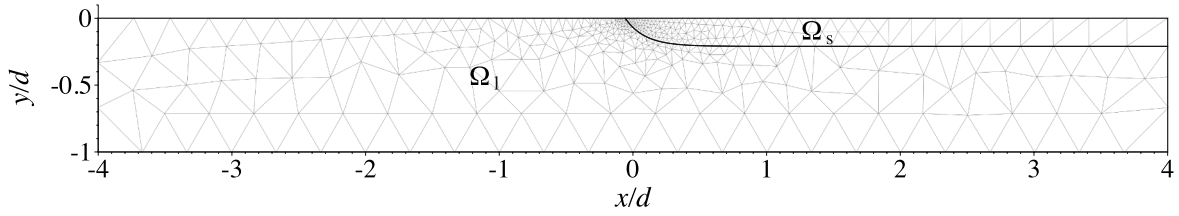

Fig. 2. Sample of the initial mesh used for numerical simulation of the HRG process.

The profile for $q_c(x)$ is modeled as a Gaussian distribution, such that

$$q_c(x) = q_{c,max}\left[\left(1-f_c\right)e^{-[(x-x_c)/w]^2 \ln 2} + f_c\right], \quad (15)$$

where $q_{c,max}$ is the peak convective heat flux, x_c is the location of the helium jet centerline, w determines the width of the heat removal profile, and $f_c q_{c,max}$ is a constant fraction of the peak convective heat flux included in the $q_c(x)$ profile to prevent the solid from melting downstream of the jet [22]. The radiative heat transfer profile is obtained as

$$q_r(x) = \varepsilon_i \sigma_b \left(T_s^4(x) - T_c^4\right), \quad (16)$$

where ε_i is the solid or liquid emissivity coefficient, σ_b is the Stefan–Boltzmann constant, $T_s(x)$ is the surface temperature at location x, and T_c is the cold far-field temperature.

The temperature distributions and the shape and position of the solid–liquid interface are determined iteratively in the numerical procedure by solving the governing equations simultaneously, until a converged steady-state solution is achieved for each set of the specified conditions.

6. Solid–liquid solution

In this study, silicon is chosen as the material of interest, with material properties listed in Table 1 [33]. All properties are assumed to be constant in the range of the investigated temperatures. Note that the density and the specific heat are assumed equal for solid and liquid silicon.

6.1. Studied cases

Three cases with different heat removal profiles and boundary conditions are studied both numerically and analytically over a range of ribbon pull speeds. The characteristic parameters in the three cases are listed in Table 2, which are chosen to be close to the experiments discussed in [28]. In all cases, the centerline of the cooling jet is positioned at $x_c = 0$ and the far-field temperature is $T_c = 300$ [K]. The width of the convective heat removal profile is equal to $w = 0.5$ [mm] and the crucible depth is equal to $d = 13$ [mm].

According to Eq. (15) for the convective heat removal rate, the values of q_s and q_l to be used in the analytical formulations are a function of the TJP position (x_{TJP}), which varies as a function of the pull speed [28]. However, because the q_c distribution is continuous at the TJP, as opposed to q_r, the heat removal difference in Eq. (7), $q_s - q_l$, can be obtained directly from Eq. (16) for the radiative heat transfer by obtaining the TJP temperature from Eq. (12). As such, the analytical temperature distribution along the solid–liquid interface, relative to the TJP temperature, can be obtained without the knowledge of x_{TJP}. For obtaining the absolute temperature distributions with the analytical formulations, the value of x_{TJP} can be extracted from numerical simulations at each pull speed.

Table 1
Silicon properties used in numerical and analytical formulations [33].

Description	Variable	Value	[Units]
Solid/liquid density	ρ	2530	[kg/m^3]
Solid/liquid spec. heat	c	1000	[J/kg K]
Solid conductivity	k_s	22	[W/m K]
Liquid conductivity	k_l	64	[W/m K]
Solid emissivity	ε_s	0.6	-
Liquid emissivity	ε_l	0.2	-
Equi. melting temp.	T_m	1685	[K]

Table 2
Characteristics parameters for the three studied cases.

Description	Variable	Case I Value	Case II Value	Case III Value	[Units]
Peak conv. heat flux	$q_{c,max}$	283	336	389	[W/cm^2]
Heat flux fraction	f_c	0.13	0.12	0.11	-
Bottom point temp.	T_b	1731	1736	1746	[K]
Top point temp.	T_t	1702	1700	1704	[K]

6.2. Numerical simulations

Samples of numerically-obtained temperature fields in the vicinity of the TJP are shown in Fig. 3 for Case II at three particular pull speeds of $u_{pull} = 0.5$ [mm/s], 1.5 [mm/s], and 2.4 [mm/s]. The adapted and refined meshes in these cases contain N_e~34k, ~26k, and ~28k total elements, respectively, in the liquid and solid domains combined. The minimum non-dimensional element size on the facet is about $\Delta x_{min}/d = 3.9 \times 10^{-5}$ for the three cases. In Fig. 3, the solidification front is shown as a solid line, over which the formed facet and its transition to roughened growth can be detected. The arrows denote the direction of a tangent to a (1 1 1) plane with a $\theta_f = 55^\circ$ angle with the free surface, which are aligned with the formed facets.

As discussed in Section 4.2, the misalignment angle at the transition point is equal to $\theta_{trans} = \sin^{-1}(K_{sn}/K_{rough}) = 1.15^\circ$. During the numerical procedure, the transition point location, and subsequently the transition or facet length (x^*_{trans}), are obtained by tracking the location on the facet at which the misalignment angle equates to this value. In the specific

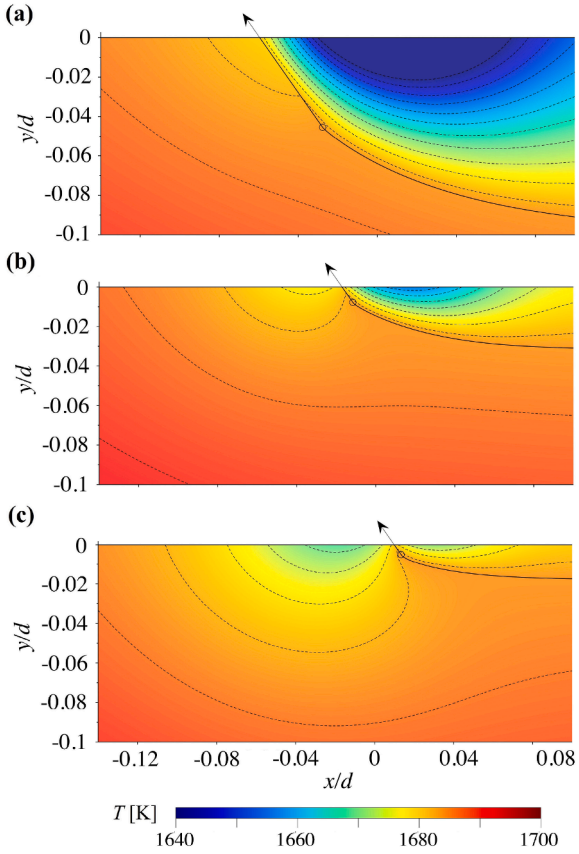

Fig. 3. Numerically-obtained temperature distributions in the vicinity of the TJP and the shape of the formed facets for Case II at a) $u_{pull} = 0.5$ [mm/s], b) $u_{pull} = 1.5$ [mm/s], c) $u_{pull} = 2.4$ [mm/s]. The dashed lines denote the contour lines, the arrows denote a tangent to the (1 1 1) plane, and the empty circles denote the transition point on the facet.

cases shown in Fig. 3, the detected transition points are marked by empty circles. It can be seen in Fig. 3 that the overall solid ribbon thickness becomes smaller as the pull speed is increased, leading to a smaller facet length and the transition point pushed toward the TJP. The ribbon thickness at the exit (right) boundary of the domain, t_{exit}, is reported in Table 3 for the three pull speeds shown in Fig. 3.

The temperature contours are displayed as dashed lines in Fig. 3. It can be clearly observed that the minimum solid temperature, $T_{s,min}$, occurs away from the TJP and close to the edge of the cooling jet at about $w/2 = 0.25$ [mm] (see Table 3). $T_{s,min}$ is increased as the pull speed is increased, because the rate of material extraction surpasses the cooling rate. Increasing the pull speed also moves the TJP position and the solidification front toward the downstream of the cooling jet center (see Fig. 1). This results in the formation of a supercooled region in the liquid, as the liquid surface becomes closer to the cooling jet. The temperature contours in Fig. 3 show the position of the local minimum liquid temperatures and the size of the supercooled regions. These values are also reported in Table 3. A more detailed discussion on the conditions leading to liquid supercooling is provided in Section 6.4.

As mentioned earlier, there is a limit for stable operation of the HRG process, called the turning point, after which the ribbon pull speed can be no longer increased [28]. The three cases of interest were investigated numerically as a function of the pull speed and the obtained results for the position of the TJP are shown in Fig. 4. The shift in the TJP position toward the downstream of the cooling jet continues until this point passes the downstream edge of the jet at $x \tilde{} 0.25$[mm], after which a stable solidification is no longer possible. Increasing the peak heat flux from Case I to Case III pushes the TJP position to the jet upstream at each pull speed, leading to a delay in reaching the turning point that occurs at $u_{pull} \simeq 1.7, 2.4$, and 2.9 [mm/s] for the three cases, respectively.

6.3. Validation of analytical estimations

A comparison of the results by the analytical formulations and the numerical simulations for the three investigated cases is shown in Fig. 5, displaying the temperature at the TJP (Fig. 5)) and the transition length of the facet (Fig. 5(b)). Note that there are no numerical data points for $u_{pull} > 1.5$ and $u_{pull} > 2.0$ in Case I and Case II, respectively, because of their maximum pull speed at the turning point shown in Fig. 4. The TJP temperature in Fig. 5(a) is about 4-5 [K] less than the equilibrium melting temperature and becomes slightly smaller in all cases as the pull speed is increased. Because both the analytical and numerical procedures use Eq. (12) for the estimation of the T_{TJP} with 2D nucleation, their results are identical at each pull speed. However, the two procedures produce different results for the transition length in Fig. 5(b).

The transition length in the analytical formulation is obtained as described in the discussion following Eq. (14). This equation predicts a smaller x^*_{trans} with increasing the pull speed. This trend is also observed in the numerical results, displayed as symbols in Fig. 5(b). The numerical results show that the transition length is increased at each pull speed as the peak convective heat flux, $q_{c,max}$, is increased from Case I to Case III (see Table 2). According to the analytical formulation of Eq. (14), x^*_{trans} is not a function of the heat flux, and therefore, the analytical result is shown as a single solid line in Fig. 5(b).

It can be observed the analytical predictions of x^*_{trans} are smaller than the obtained numerical results for all pull speeds. The main reason behind this difference is the fact that the analytical assumptions are only valid close to the TJP in the limit of $r < \epsilon$. For the constant heat flux assumption for both the liquid and solid at the TJP, the radius of analysis must be considerably smaller than the cooling jet width, such that $r/w \tilde{} \mathcal{O}(0.1)$.

Table 3
Results of the numerical simulation at three pull speeds in Case II.

Description	Variable	$u_{pull} = 0.5$ [mm/s] Value	$u_{pull} = 1.5$ [mm/s] Value	$u_{pull} = 2.4$ [mm/s] Value	[Units]
Maximum ribbon thick.	t_{exit}	2.6	1.1	0.70	[mm]
Min. solid temp.	$T_{s,min}$	1607.7	1654.2	1670.7	[K]
Min. liquid temp.	$T_{l,min}$	1680.6	1677.1	1668.0	[K]
Min. solid temp. pos.	$x_{s,min}$	0.13	0.23	0.39	[mm]
Min. liquid temp. pos.	$x_{l,min}$	−0.78	−0.42	−0.24	[mm]
TJP pos.	x_{TJP}	−0.77	−0.22	0.19	[mm]

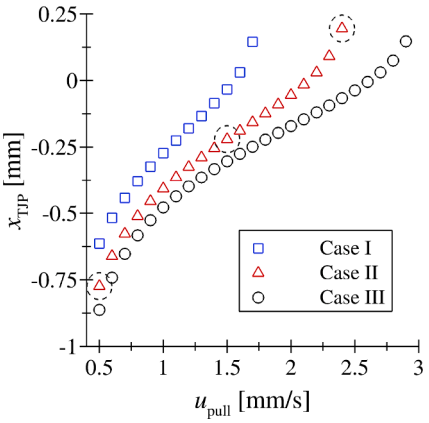

Fig. 4. Results of the numerical simulation for the triple junction position as a function of the pull speed in the three investigated cases. The dashed circles denote the specific cases shown in Fig. 3.

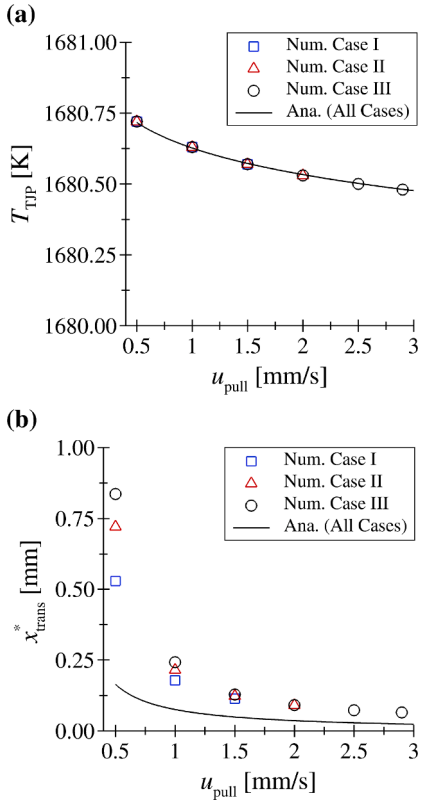

Fig. 5. Comparison of analytical and numerical results for the three investigated cases, showing a) the obtained temperature at the TJP and b) the obtained transition length.

For all the investigated cases in this study, this means a radius of $r < 0.05$ [mm]. At this radius, the maximum Pe number with $u_{pull} = 3.0$ mm/s is $Pe_{max} = 0.006$, which confirms that ignoring the convective term in Eq. 2 at this scale is accurate. However, all the numerically-obtained transition lengths in Fig. 5(b) are larger than $r/w \tilde{} 0.1$. It can be concluded that the analytical assumptions are not valid over the entire length of the facet. The analytical results are expected to be applicable to a larger portion of the facet length at larger pull speeds, as the ribbon thickness and the facet length become smaller. In spite of this, the analytical predictions do qualitatively predict the behavior of the facet length as a function of the pull speed.

The numerically-obtained temperature distributions along the facet are shown in Fig. 6(a) for Case II at three different pull speeds. It can be observed that all temperature distributions approach the TJP with a positive and finite slope, which is in agreement with the analytical prediction shown in Eq. 7. However, the numerical facet temperatures deviate from a linear variation as the distance from the TJP is increased, mainly because r/w is no longer small. At large pull speeds ($u_{pull} > 1.0$ [mm/s]), the temperature monotonically increases along the facet. However at small pull speeds, the temperature remains nearly constant for a portion of the facet length (see the blue squares in Fig. 6 (a)), before increasing to the equilibrium melting temperature of $T_m = 1685$ [K] toward the end of the facet.

For a more quantitative comparison, the temperature gradient in the facet direction at the TJP, $(dT/dx^*)_{TJP} = a^*$, is obtained both numerically and analytically as a function of the pull speed and is shown in Fig. 6(b) for all investigated cases. Note that the analytical gradient is only a function of the jump in heat flux at the TJP ($q_s - q_l$) and not the peak heat flux. The heat flux jump is only a function of T_{TJP}, which is nearly constant for all cases. As such, the analytical result is shown as a single solid line in Fig. 6(b). It can be observed that a^* increases in both numerical and analytical results as the pull speed is increased, as predicted by the analytical formulation of Eq. (7). The numerical gradients (the empty symbols) are nearly equal for the three cases at each pull speed, but smaller than the analytical prediction.

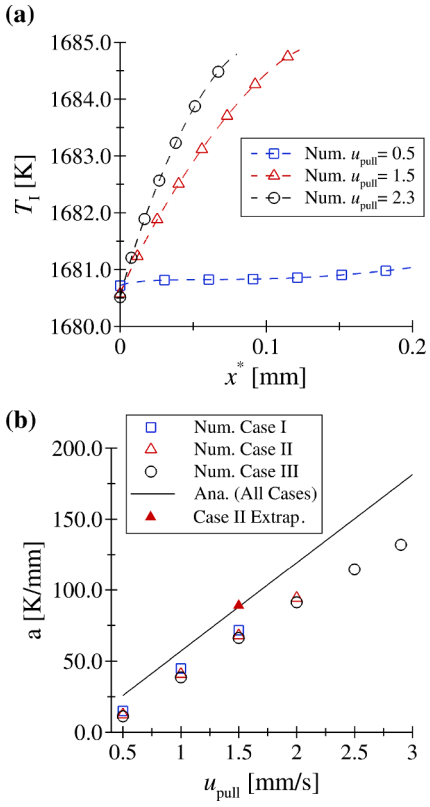

Fig. 6. Temperature profiles along the facet, with a) numerical temperature distributions for Case II as a function of the pull speed and b) numerical and analytical temperature gradients at the TJP for all investigated cases. The symbols in panel (a) are down-sampled. The solid red triangle in panel (b) denotes the result of the grid refinement and extrapolation performed on the solution of Case II at $u_{pull} = 1.5$ [mm/s] shown in Table 4.

The difference in temperature gradient between the analytical prediction and the numerical simulations is due to the mesh resolution at the TJP in the investigated numerical model. To prove this, a grid study is performed on a sample data point in Case II with $u_{pull} = 1.5$ [mm/s]. This base case has a grid size of $N_e \tilde{} 28$k elements. The base mesh is uniformly refined twice and the three parameters of TJP position, x_{TJP}, transition length, x^*_{trans}, and temperature gradient, a^*, are obtained and reported in Table 4. Moreover, a Richardson extrapolation procedure is performed on the reported parameters, based on the method outlined in reference [34], and the resulting extrapolated values are reported. For reference, the analytically predicted values are also shown in Table 4. Note that the analytical formulation does not predict the TJP position.

It is observed that x_{TJP} and x^*_{trans} values are already converged in the base mesh size. The temperature gradient on the other hand, slowly converges to an extrapolated value of $a^*_{num} = 88.91$ [K/mm], shown as a solid triangle in Fig. 6(b), with a convergence rate of 0.15. Comparing to the analytically-predicted temperature gradient of $a^*_{ana} = 88.03$ [K/mm], the relative difference of the two analyses is less than 1%. Therefore, it is clear that the reason for the difference between the analytical and numerical solutions in Fig. 6(b) is numerical error.

It can be concluded that the analytical formulations can well predict the behavior of the TJP. This suggests that a simplified analytical formulation can replace numerical procedures for a preliminary evaluation of the HRG processes and an analysis of their thermal stability.

6.4. Supercooling in the liquid domain

An important outcome of the analytical formulation for the HRG processes is the prediction of existence of a supercooled region in the liquid upstream of the TJP. This prediction is important because it can be an indication of thermal instability in the problem [13]. The liquid adjacent to the TJP will be always supercooled if its temperature gradient in the x direction is positive, $dT/dx > 0$. Note that it is also possible to have a supercooled region close to the TJP without a positive temperature gradient, since T_{TJP} is itself less than the equilibrium melting temperature, as displayed in Fig. 5(a).

Referring to Eq. (9), the pull speed required for a positive temperature gradient in the liquid can be stated as

$$u_{pull} > \frac{q_s - q_l}{\rho L_f}\left[\cot(\theta_f) + \tan(\theta_f)\right] + \frac{q_l(k_l - k_s)}{\rho L_f k_l}\tan(\theta_f). \quad (17)$$

It was previously discussed that the jump in heat flux, $q_s - q_l$, can be directly obtained by computing the TJP temperature from Eq. (12) and computing the radiative heat flux difference from the liquid and the solid at the TJP from Eq. (16). Because the TJP temperature is nearly constant over the investigated range of pull speeds in Fig. 5(a), $q_s - q_l$ can be assumed constant as well. Consequently, the minimum pull speed for a supercooled liquid in Eq. (17) can be stated as a linear function of the total heat flux from the liquid at the TJP, such that $u_{pull,min} = \alpha + \beta q_l$. The minimum pull speed is plotted as a function of q_l in Fig. 7, displayed as a solid black line. It can be observed that $u_{pull,min}$ increases slightly as q_l is increase, meaning that for higher heat fluxes liquid supercooling occurs at larger pull speeds.

It was previously observed in the temperature plots of Fig. 3 that increasing the pull speed results in a larger and colder supercooled region in the liquid. The values of q_l in the numerical simulations of the three investigated cases are obtained as a function of the pull speed and shown as symbols in Fig. 7. Note that q_l is a function of the TJP position, which is in turn a function of the pull speed (see Eq. (15) and Fig. 4).

Table 4
Grid study performed on the numerical simulation of Case II with $u_{pull} = 1.5$ [mm/s]. Note that only 4 significant digits are shown.

Description	Variable	Base case Value	1st Refine. Value	2nd Refine. Value	Extrap. Value	Analytical Value	[Units]
Grid size	N_e	28k	111k	446k	–	–	elements
Min. element size	Δx_{min}	5.1×10^{-4}	2.5×10^{-4}	1.2×10^{-4}	–	–	[mm]
TJP position	x_{TJP}	−0.3037	−0.3037	−0.3037	−0.3037	–	[mm]
Transition length	x^*_{trans}	0.1285	0.1287	0.1287	0.1287	0.0492	[mm]
Temp. gradient	a^*	66.09	68.40	70.47	88.91	88.03	[K/mm]

Consequently, q_l increases to a maximum as the TJP crosses the cooling jet center and decreases afterwards. For example, the liquid heat flux for the three pull speeds in Fig. 3 is equal to $q_l = 155$ [W/cm^2],292 [W/cm^2], and 305 [W/cm^2], respectively.

In Fig. 7, all the data points from the numerical simulations are above the $u_{pull,min}$ line, meaning that there must be a supercooled region in the liquid in all the numerically-investigated cases. This was confirmed in Fig. 3 for Case II, even at the smallest pull speed. At small pull speeds, the numerical data points are extremely close to the $u_{pull,min}$ line, leading to a small supercooled region (see Fig. 3(a)). As the pull speed is increased in each numerical case, it gets farther from the analytically-predicted minimum pull speed, leading to a larger amount of supercooling. In the specific case shown in Fig. 3(b) with $u_{pull} = 1.5$ [mm/s], the minimum pull speed corresponding to the same value of q_l is equal to $u_{pull,min} = 0.68$ [mm/s]. It can be concluded that the liquid heat flux at the TJP must be relatively large for a specific pull speed to ensure that no supercooling occurs in the liquid.

7. Conclusions

The solidification mechanism during the horizontal ribbon growth process was studied analytically and numerically in this study with an emphasis on the triple junction point (TJP), where the solid ribbon, the liquid, and the surrounding gas meet. The HRG process was analytically formulated in the vicinity of the TJP, incorporating the solidification kinetics, and the temperature distributions in the solid, the liquid, and along their interface were obtained. It was shown that the solidification is initiated with 2D nucleation at the TJP and proceeds with propagation of steps along the solidification front, which forms a facet with a nearly constant angle. The behavior of the solidification facet was examined in the vicinity of the TJP as a function of the material properties, the ribbon pull speed, and the cooling heat flux from the free surfaces. Using the analytical formulation, the temperature distribution along the facet, the facet length, and the existence of a supercooled region in the liquid can be predicted.

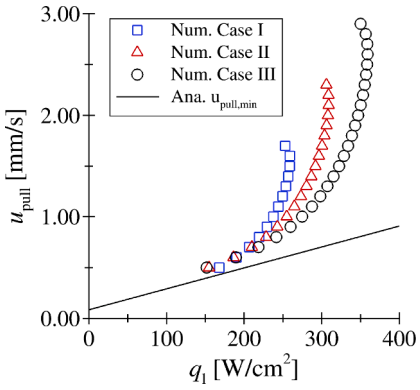

Fig. 7. Minimum pull speed resulting in a supercooled region in the liquid domain as a function of the total heat flux from the liquid at the TJP. The symbols denote the liquid heat flux at each pull speed in the three numerically-investigated cases.

The solid–liquid problem was also simulated numerically using an accurate *hp*-finite element formulation that incorporates the solidification kinetics. It was observed that increasing the ribbon pull speed shifts the TJP toward the downstream of the cooling jet, increases the minimum temperature in the solid, and results in a larger and colder supercooled region in the liquid. Comparison of the numerical and analytical results showed that the assumptions of the analytical formulation are not valid over the entire facet length, especially at small pull speeds. However, the analytical formulation proved to successfully predict the behavior of the HRG process in the vicinity of the TJP, where the solidification process is initiated and the thermal stability of the problem is dictated. These findings suggest that the proposed analytical model can be used in lieu of numerical simulations to investigate the HRG process as a function of the underlying parameters that are involved.

CRediT authorship contribution statement

Alireza Pirnia: Methodology, Validation, Investigation, Writing - original draft. **Brian T. Helenbrook:** Conceptualization, Software, Writing - review & editing, Supervision, Funding acquisition, Project administration.

Declaration of Competing Interest

The authors declare that they have no known competing financial interests or personal relationships that could have appeared to influence the work reported in this paper.

Acknowledgments

This material is based upon work supported by the National Science Foundation (NSF) under Grant No. 1762802.

References

[1] M. Narayanan, T. Ciszek, Silicon solar cells: Materials, devices, and manufacturing, Springer Handb, Cryst. Growth (2010) 1701–1718, https://doi.org/10.1007/978-3-540-74761-1_51.
[2] L. Arnberg, M. Di Sabatino, E.J. Øvrelid, State-of-the-art growth of silicon for PV applications, J. Cryst. Growth 360 (2012) 56–60, https://doi.org/10.1016/j.jcrysgro.2012.03.024.
[3] J. Derby, R. Brown, Thermal-capillary analysis of Czochralski and liquid encapsulated czochralski crystal growth: I. simulation, J. Cryst. Growth 74 (1986) 605–624, https://doi.org/10.1016/0022-0248(86)90208-3.
[4] O. Weinstein, W. Miller, Three-dimensional calculations of facets during czochralski crystal growth, J. Cryst. Growth 312 (2010) 989–996, https://doi.org/10.1016/j.jcrysgro.2009.12.071.
[5] K. Ravi, The growth of efg silicon ribbons, J. Cryst. Growth 39 (1977) 1–16, https://doi.org/10.1016/0022-0248(77)90151-8.
[6] M. Muller, B. Birkmann, F. Mosel, I. Westram, A. Seidl, Silicon EFG process development by multiscale modeling, J. Cryst. Growth 312 (2010) 1397–1401, https://doi.org/10.1016/j.jcrysgro.2009.09.021.
[7] W. Shockley, Process for growing single crystals, http://www.google.com/patents/US3031275, 1962. US Patent 3,031,275.
[8] C. Bleil, A new method for growing crystal ribbons, J. Cryst. Growth 5 (1969) 99–104, https://doi.org/10.1016/0022-0248(69)90020-7.
[9] T. Ciszek, Photovoltaic silicon crystal growth, Bulk Cryst. Growth Electron. Opt. OptoElectron. Mater. (2005) 451–476, https://doi.org/10.1002/9780470012086.ch16.

[10] G.A. Oliveros, R. Liu, S. Sridhar, B.E. Ydstie, Silicon wafers for solar cells by horizontal ribbon growth, Ind. Eng. Chem. Res. 52 (2013) 3239–3246, https://doi.org/10.1021/ie301857p.
[11] B. Kudo, Improvements in the horizontal ribbon growth technique for single crystal silicon, J. Cryst. Growth 50 (1980) 247–259, https://doi.org/10.1016/0022-0248(80)90248-1.
[12] H. Bates, D. Jewett, Low angle silicon sheet growth: A review of progress, problems and promise, in: Flat-Plate Solar Array Proj. Res. Forum on the High-Speed Growth and Characterization of Crystals for Solar Cells, vol. 1, 1984, pp. 297–307.
[13] B.T. Helenbrook, N.S. Barlow, Spatial–temporal stability analysis of faceted growth with application to horizontal ribbon growth, J. Cryst. Growth 454 (2016) 35–44, https://doi.org/10.1016/j.jcrysgro.2016.08.052.
[14] S. Schiaffino, A.A. Sonin, On the theory for the arrest of an advancing molten contact line on a cold solid of the same material, Phys. Fluids 9 (1997) 2227–2233, https://doi.org/10.1063/1.869345.
[15] R. Li, N. Ashgriz, S. Chandra, J.R. Andrews, Solidification contact angles of molten droplets deposited on solid surfaces, J. Mater. Sci. 42 (2007) 9511–9523, https://doi.org/10.1007/s10853-007-1757-9.
[16] T.V. Vu, Q.H. Luu, Containerless solidification of a droplet under forced convection, Int. J. Heat Mass Transfer 143 (2019), https://doi.org/10.1016/j.ijheatmasstransfer.2019.118498.
[17] S. Nishio, Y. Mitani, K. Shibuya, Stability of contact line accompanied by solidification, Heat Transfer Japanese Res. 26 (1997) 360–371, https://doi.org/10.1002/(SICI)1520-6556(1997)26:6<360::AID-HTJ2>3.0.CO;2-U.
[18] T. Ciszek, Techniques for the crystal growth of silicon ingots and ribbons, J. Cryst. Growth 66 (1984) 655–672, https://doi.org/10.1016/0022-0248(84)90166-0.
[19] T. Duffar (Ed.), Crystal Growth Processes Based on Capillarity: Czochralski, Floating Zone, Shaping, and Crucible Techniques, John Wiley & Sons, 2010.
[20] N. Eustathopoulos, B. Drevet, S. Brandon, A. Virozub, Basic principles of capillarity in relation to crystal growth, Cryst. Growth Processes Capillarity (2010) 1–49, https://doi.org/10.1002/9781444320237.ch1.
[21] T. Surek, B. Chalmers, The direction of growth of the surface of a crystal in contact with its melt, J. Cryst. Growth 29 (1975) 1–11, https://doi.org/10.1016/0022-0248(75)90041-X.
[22] B.T. Helenbrook, Solidification along a wall or free surface with heat removal, J. Cryst. Growth 418 (2015) 79–85, https://doi.org/10.1016/j.jcrysgro.2015.02.028.
[23] G.A. Oliveros, S. Sridhar, B.E. Ydstie, Existence and static stability of the meniscus in horizontal ribbon growth, J. Cryst. Growth 411 (2015) 96–105, https://doi.org/10.1016/j.jcrysgro.2014.09.036.
[24] J. Zoutendyk, Theoretical analysis of heat flow in horizontal ribbon growth from a melt, J. Appl. Phys. 49 (1978) 3927–3932, https://doi.org/10.1063/1.325401.
[25] C. Rhodes, M. Sarraf, C. Liu, Investigation of the meniscus stability in horizontal crystal ribbon growth, J. Cryst. Growth 50 (1980) 94–101, https://doi.org/10.1016/0022-0248(80)90234-1.
[26] J. Xu, D. Shen, T. Sun, J. Ding, N. Yuan, Modeling and analysis of novel horizontal ribbon growth of silicon crystal, Crystals 8 (2018) 36, https://doi.org/10.3390/cryst8010036.
[27] D. Anderson, S. Davis, Fluid flow, heat transfer, and solidification near tri-junctions, J. Cryst. Growth 142 (1994) 245–252, https://doi.org/10.1016/0022-0248(94)90293-3.
[28] B.T. Helenbrook, P. Kellerman, F. Carlson, N. Desai, D. Sun, Experimental and numerical investigation of the horizontal ribbon growth process, J. Cryst. Growth 453 (2016) 163–172, https://doi.org/10.1016/j.jcrysgro.2016.08.034.
[29] P. Kellerman, B. Kernan, B.T. Helenbrook, D. Sun, F. Sinclair, F. Carlson, Floating silicon method single crystal ribbon – observations and proposed limit cycle theory, J. Cryst. Growth 451 (2016) 174–180, https://doi.org/10.1016/j.jcrysgro.2016.07.012.
[30] O. Weinstein, S. Brandon, Dynamics of partially faceted melt/crystal interfaces I: computational approach and single step–source calculations, J. Cryst. Growth 268 (2004) 299–319, https://doi.org/10.1016/j.jcrysgro.2004.04.108.
[31] A. Virozub, S. Brandon, Is it important to account for heat transport and interfacial attachment kinetics when calculating the shape of directionally solidified drops? J. Cryst. Growth 312 (2010) 2472–2478, https://doi.org/10.1016/j.jcrysgro.2010.05.025.
[32] B. Helenbrook, J. Hrdina, High-order adaptive arbitrary-lagrangian–eulerian (ale) simulations of solidification, Comput. Fluids 167 (2018) 40–50, https://doi.org/10.1016/j.compfluid.2018.02.028.
[33] M. Mito, T. Tsukada, M. Hozawa, C. Yokoyama, Y.-R. Li, N. Imaishi, Sensitivity analyses of the thermophysical properties of silicon melt and crystal, Meas. Sci. Technol. 16 (2005) 457, https://doi.org/10.1088/0957-0233/16/2/018.
[34] (July 22, 2008), Procedure for Estimation and Reporting of Uncertainty Due to Discretization in CFD Applications, J. Fluids Eng. 130 (2008). doi:10.1115/1.2960953, 078001.